Testing mode-coupling predictions for α and β relaxation in $Ca_{0.4}K_{0.6}(NO_3)_{1.4}$ near the liquid-glass transition by light scattering

G. Li, W.M. Du, X.K. Chen, and H.Z. Cummins
Department of Physics, City College of New York, CUNY, New York, New York 10031

N.J. Tao
Department of Physics, Arizona State University, Tempe, Arizona 85287
(Received 3 September 1991)

Light-scattering studies of the liquid-glass transition of $Ca_{0.4}K_{0.6}(NO_3)_{1.4}$ have been carried out from 305 to 23 °C. Composite spectra covering over four decades in frequency were obtained by combining data obtained with a Sandercock tandem Fabry-Pérot interferometer and Raman spectra. Two-step relaxation processes were observed in the supercooled liquid near the glass transition. The α relaxation exhibits a temperature-independent stretching for $T > T_c$ with $T_c \approx 105$ °C, which is about 45 °C above the glass transition temperature. The β-relaxation frequency scale indicates critical slowing down when the temperature approaches T_c from either above or below. Scaling analyses for both α and β relaxations provide good agreement with the predictions of mode-coupling theory.

PACS number(s): 64.70.Pf, 78.35.+c, 46.30.Jv

I. INTRODUCTION

The liquid-glass transition has been the subject of extensive experimental and theoretical study for many years, but the fundamental nature of the transition is still not fully understood. During the past several years a theoretical approach was formulated based on a self-consistent treatment of nonlinear interactions between density fluctuation modes in the mode-coupling approximation within the framework of the Mori-Zwanzig formalism. This mode-coupling theory (MCT) predicts an ideal kinetic glass transition and leads to various nontrivial qualitative and quantitative predictions that are experimentally accessible [1, 2]; for a review, see Ref. [3]. These predictions have stimulated a number of experimental studies, including the work being reported here.

Taking the normalized density correlation function $\Phi(t)$ as the dynamical variable, MCT models the density fluctuation relaxation kernel of generalized hydrodynamics using first-, second-, or higher-order nonlinear interactions. The self-consistent solutions of the MCT predict that even for a simple hard-sphere or Lennard-Jones system [2, 4] when the temperature is lowered toward a crossover temperature T_c, which is somewhat above the calorimetric glass transition temperature T_g, structural relaxation experiences rapid slowing down. The fluctuations then exhibit two-step relaxation with scaling properties which can be characterized by sets of power laws with nontrivial exponents for the different frequency ranges [5–10].

The ideal kinetic glass transition at T_c predicted by the simple versions of the MCT does not occur because ergodicity is restored by activated hopping processes which were not included in the original formulation. The transition is smeared out by these processes and the primary α relaxation continues until T_g, where the system falls out of equilibrium. As we shall show below, however, although the low-frequency dynamics near T_g are dominated by the topology of the energy surface, high-frequency dynamics appear to be primarily controlled by the anharmonic processes contained in the MCT, even in the glass phase below T_g. Indeed, for dynamics above $\sim 3 \times 10^8$ Hz, the ideal glass transition predicted by the MCT turns out to be of greater importance than the calorimetric glass transition at T_g.

It is well known that near the liquid-glass transition, the dynamics of the density fluctuations extend for several orders of magnitude in time or frequency due to the slowing down of the relaxation processes. Therefore, in order to observe the whole dynamic process, one has to measure the relaxation spectra over a large frequency (or time) window which covers the whole dynamic range. Such large-spectral-range experimental observations have usually been limited by insufficient instrumental resolution or response. An important exception is a recent neutron-scattering study of $Ca_{0.4}K_{0.6}(NO_3)_{1.4}$ (CKN), which showed a complete picture of both the low- and high-frequency dynamics near the liquid-glass transition by combining neutron spin-echo (NSE) and time-of-flight (TOF) data [11]. Covering a frequency range of more than four decades, the data exhibit two relaxation processes and the scaling properties predicted by the MCT. But the data processing involved in joining the NSE and TOF data and the existence of a gap between the NSE and TOF measurements may complicate the analysis.

By exploiting a Sandercock tandem Fabry-Pérot interferometer (TFPI) Brillouin scattering apparatus, which has the advantages of suppressing neighboring orders and permitting rapid adjustment of the free spectral range, and combining several Brillouin spectra of different free spectral ranges for each temperature with a Raman spectrum, we were able to obtain low-frequency dynamic

light-scattering spectra which cover a frequency range of more than four decades. With this wide-frequency-range data, we are able to observe the overall evolution of both the α and β relaxations in CKN and to quantitatively test some important predictions of the MCT.

Several central predictions of the MCT are of interest: the prediction of two relaxation processes (α and β relaxations) in the supercooled liquid near the glass transition; the stretching of the α relaxation, and the scaling properties of the α relaxation above T_c and β relaxation both above and below T_c. Some of the MCT predictions have been tested previously by various experimental and computer-simulation studies [12–14]. The neutron-scattering results of Mezei, Knaak, and Farago [15] and Knaak, Mezei, and Farago [11] explored the scaling property of the α relaxation, the existence of the two-step relaxation process, and the scaling behavior of the β relaxation above T_c. The scaling property of the α relaxation of glass-forming systems has also been studied by other groups [16–19]. Recently Doster, Cusack, and Petry [20] reported a neutron-scattering study and MCT analysis of the β relaxation in a globular protein near T_c. The β relaxation scaling has also been tested by experimental studies of dielectric measurements for polymers [21, 22] and dynamic light-scattering studies of hard spherical colloids [23]. These results are generally in good agreement with the MCT.

In spite of the intensive experimental studies of glass transitions, no experimental results have yet been reported concerning the dynamics of the β relaxation in the temperature range between T_g and T_c, which may provide a crucial test for the MCT below T_c.

It has been predicted by a recently developed percolation theory [24–28] that the stretching of the α relaxation is a temperature-dependent phenomenon that can be described by a temperature-dependent $\beta(T)$, where β is the exponent of the stretched exponential (or Kohlrausch) function $\exp[-(t/\tau)^{\beta}]$. This theory predicted that β is $\frac{1}{3}$ at the glass transition temperature T_g and continuously increases toward 1 with increasing temperature. This prediction of temperature-dependent stretching of α relaxation is in contradiction with the MCT, which predicts a temperature-independent α-relaxation stretching above T_c. Experimental determination of the temperature dependence of the α-relaxation stretching, or equivalently of the exponent $\beta(T)$, can provide a direct test for these competing theoretical predictions.

To explore the dynamics of the liquid-glass transition and to test the particular predictions mentioned above, we carried out wide-frequency-range light-scattering studies of the much studied ionic glass former $Ca_{0.4}K_{0.6}(NO_3)_{1.4}$ near the glass transition temperature. The experimental results were analyzed and compared with the predictions of the MCT. The results are presented in the following sections.

II. EXPERIMENT

High-purity KNO_3 (99.999%) and $Ca(NO_3)_2{\cdot}4H_2O$ (99.9995%) were obtained from Alfa Products. $Ca(NO_3)_2{\cdot}4H_2O$ was dried in a ceramic crucible by slowly heating it to $\sim$ 300 °C for a few hours and was then mixed with the appropriate amount of KNO_3 to obtain $Ca_{0.4}K_{0.6}(NO_3)_{1.4}$.

To clean the sample, we first transferred the molten mixture to another crucible using a glass pipette. Most of the visible dust sticks on the inner wall of the first container. To prepare the highest-quality samples, we dissolved the solidified mixture by adding purified water after it was cooled to room temperature. The solution was filtered with a 0.1-μm MSI (Micron Separations, Inc.) filter and transferred into a glass tube of $\sim$ 1.5-cm diam. The sample was then slowly heated in vacuum to evaporate the water. After most of the water was evaporated, the sample was thermally cycled by cooling to room temperature and then heating up to $\sim$ 400 °C several times. In each cycle the sample was kept at $\sim$ 400 °C for $\sim$ 24 h. The samples obtained with this procedure were very clean and no crystallization occurred even when a sample was cooled down to the glass state very slowly.

The glass tube filled with purified CKN was then sealed with teflon tape and mounted in a custom-made Oxford high-temperature furnace with optical windows. A thermocouple was installed inside the furnace close to the sample. The temperature was controlled by an Oxford ITC4 temperature controller. The temperature of the sample was calibrated against the reading of a thermocouple placed inside a dummy sample cell. The accuracy of the temperature measurement was about ± 2 °C.

The light-scattering measurements were performed in VH scattering geometry. To avoid the influence of Brillouin scattering from the transverse acoustic mode in the low-temperature measurements, a large-scattering angle ($\theta = 173°$) was used since the Brillouin scattering intensity of the transverse acoustic mode goes to zero when θ approaches 180°. The Brillouin scattering apparatus, which is based on a six-pass Sandercock-tandem Fabry-Pérot interferometer, has been described in a previous publication [29]. The Spectra Physics argon ion laser was operated at 4880 Å, and the typical laser power used was $\sim$ 50 mW. To obtain spectra of different spectral ranges, four different mirror separations ($d = 0.5, 3.5, 10$, and 25 mm) were used and the frequency bandpass width of the Amici prism bandpass filter was matched for each separation. Spectra were collected in the temperature range of 305 to 23 °C. The typical collection time for each spectrum was about 20 min.

The high-frequency parts of the spectra were obtained by Raman-scattering spectroscopy of the same sample in the same scattering geometry, and at the same temperatures as for the Brillouin scattering experiments. The conventional Raman-scattering apparatus has also been described previously [30]. The laser power used was $\sim$ 300 mW.

III. EXPERIMENTAL RESULTS

To obtain spectra spanning a wide frequency range, we combined spectra obtained with different free spectral ranges. To do this, each Brillouin spectrum was first averaged over the Stokes and anti-Stokes sides to obtain

a half spectrum with only positive frequencies. Then the Brillouin spectra with different spectral ranges and the Stokes Raman spectrum collected at the same temperature were combined by matching their overlap regions. In doing this, we used the set of Brillouin spectra obtained with $d = 3.5$ mm as a standard for intensities; special attention was paid to the consistency and continuity of this set during the data collection. The composite spectra are shown in Fig. 1, in which the number of data points on each spectrum has been reduced according to a logarithmic scale. The small bumps near 20 GHz are due to leakage of the longitudinal acoustic Brillouin components through the imperfect polarizer.

The spectra cover a frequency range of more than four decades (0.3 GHz–6 THz). The overall shape of the spectra is similar to the neutron-scattering results [11]. They exhibit an evolution of the low-frequency relaxation from the liquid state to the glass state. The spectra near and above 100 °C clearly display two adjacent power-law regions, which is an indication of a two-step relaxation process. The two-step relaxation process is more clearly seen in the plot of the imaginary part of the effective susceptibility $\tilde{\chi}(\omega)$ as displayed in Fig. 2, which was obtained by dividing the intensity spectra shown in Fig. 1 by the Bose factor:

$$\tilde{\chi}''(\omega) = I(\omega)/[n(\omega) + 1] . \tag{3.1}$$

[Equation (3.1) is essentially equivalent to $\tilde{\chi}''(\omega) = (\omega/k_B T)I(\omega)$ for $\omega \leq 700$ GHz in the temperature range of interest.] The low-frequency peaks visible in the high-temperature effective susceptibility curves indicate the primary relaxation process (which is actually the convoluted result of the α relaxation for the density fluctuations, as we will discuss in later sections). The high-frequency peak visible at all temperatures is the microscopic excitation band. The crossover frequency of the

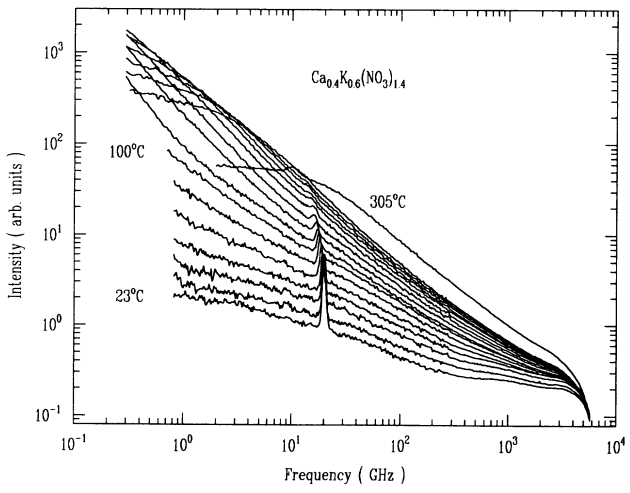

FIG. 1. Composite depolarized $\theta = 173°$ Brillouin and Raman-scattering spectra of CKN. The temperatures are (top to bottom) 305, 195, 180, 170, 160, 150, 140, 130, 120, 110, 100, 90, 80, 70, 60, 45, and 23 °C. The small peaks appearing at $\sim$ 20 GHz are due to leakage of the LA Brillouin components.

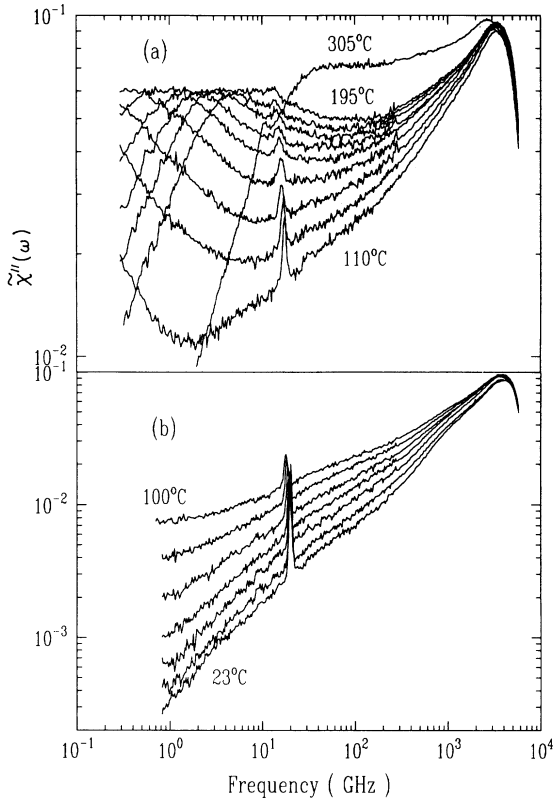

FIG. 2. Effective susceptibility spectra corresponding to Fig. 1 obtained with Eq. (3.1): (a) $T = 305$, 195, 180, 170, 160, 150, 140, 130, 120, and 110 °C (top to bottom). (b) $T = 100$, 90, 80, 70, 60, 45, and 23 °C (top to bottom).

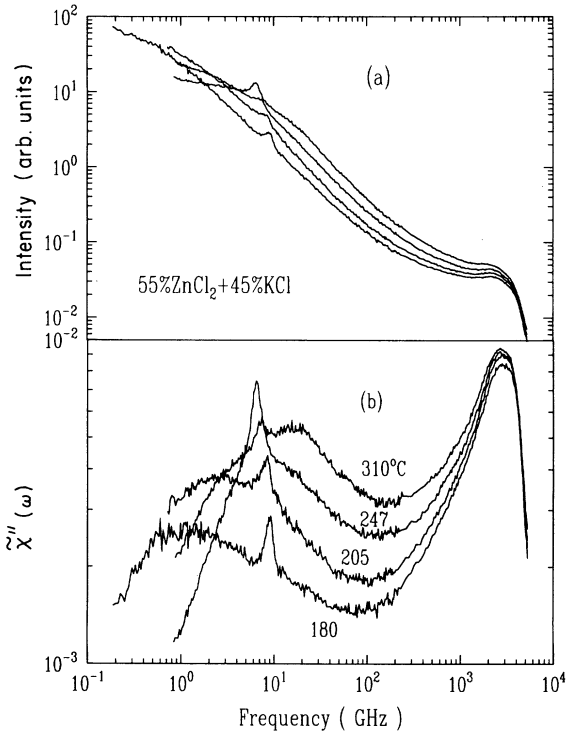

FIG. 3. Depolarized light-scattering spectra (a) and effective susceptibility spectra (b) of 55 mol %$ZnCl_2$ +45 mol %KCl. The temperatures are (top to bottom) 310, 247, 205, and 180 °C.

two power-law regions can be identified as the minimum of the susceptibility curves between the low-frequency peak and the microscopic high-frequency peak. These curves are very similar to the MCT calculated results shown in Fig. 2 of Ref. [6].

Measurements with $\theta = 90°$ scattering geometry were also performed at a few temperatures with results essentially the same as the $\theta = 173°$ results, except that strong TA modes were superimposed on the continuous spectra. Therefore the results shown in Figs. 1 and 2 are essentially wave-vector-independent in the small-q limit.

To examine the possibility that the spectral shapes of Figs. 1 and 2 are due to the rotational contribution of the NO_3 group, we performed similar ($\theta = 90°$) measurements on a monatomic viscous liquid, 55 mol %$ZnCl_2$ + 45 mol %KCl, which presumably produces no rotational contribution [31, 32]. The spectra and the susceptibility obtained from 310 to 180 °C are shown in Fig. 3. The spectral shapes are seen to be similar to those of Figs. 1 and 2 for temperatures well above T_c. This similarity implies that the results shown in Figs. 1 and 2 represent the general structural dynamics of viscous liquids.

IV. THEORY

A. Mode-coupling-theory predictions

The fundamental dynamical quantity of the mode-coupling theory for the liquid-glass transition is the normalized density correlation function

$$\Phi_q(t) = < \delta\rho_q(0)\delta\rho_q(t) > /S_q \ , \tag{4.1}$$

where $\delta\rho_q$ is the qth Fourier component of the microscopic density fluctuation, and $S_q = < |\delta\rho_q|^2 >$ is the static structure factor. $\Phi_q(t)$ obeys a generalized oscillator equation of motion:

$$\ddot{\Phi}_q(t)+\gamma_0\Omega_q^2\dot{\Phi}_q(t)+\Omega_q^2\Phi_q(t)+\Omega_q^2\int_0^t d\tau\, m_q(t-\tau)\dot{\Phi}_q(\tau) = 0 \ , \tag{4.2}$$

with initial conditions $\Phi_q(t = 0) = 1$, $\dot{\Phi}_q(t = 0) = 0$. This equation of motion is equivalent to

$$\Phi_q(z) = -1/(z - \Omega_q^2/\{z + \Omega_q^2[i\gamma_0 + m_q(z)]\}) \ , \tag{4.3}$$

where $\Phi_q(z)$ is the Laplace transform of $\Phi_q(t)$ with complex frequency z [$\Phi_q(z) = i\int_0^\infty \Phi_q(t)e^{izt}dt$], Ω_q is the microscopic frequency ($\Omega_q^2 = v^2q^2/S_q$), γ_0 is a regular damping constant, and $m_q(z)$ is the current relaxation kernel.

The equations of motion are closed by expressing the kernel in terms of products of one, two, or more correlators,

$$m_q(t) = \sum_{q_1} V^{(1)}(q,q_1)\Phi_{q_1}(t) + \sum_{q_1,q_2} V^{(2)}(q,q_1,q_2)\Phi_{q_1}(t)\Phi_{q_2}(t) + \cdots \ , \tag{4.4}$$

where the vertex $V^{(i)}$ is expressed in terms of the structure factor S_q [2]. If the system is cooled in the liquid phase, the vertices increase and there appears a critical temperature T_c where a dynamical phase transition from ergodic liquid dynamics for $T > T_c$ to nonergodic glass dynamics for $T < T_c$ occurs. The analytic results of the MCT deal primarily with the solution of Eqs. (4.2) and (4.4) for small separation parameter $\epsilon \propto (T_c - T)/T_c$. Actually, the theory is more complicated because of the ergodicity restoring activated processes [6, 7], but this aspect will not be discussed here.

From the MCT, the slowing down of the dynamics of the density fluctuation near the critical temperature T_c is governed by two scaling frequencies,

$$\omega_\epsilon \propto \Omega|\epsilon|^{1/2a} \ , \tag{4.5a}$$

$$\omega'_\epsilon \propto \Omega|\epsilon|^{\gamma} \ , \tag{4.5b}$$

where $\gamma = 1/2a + 1/2b$. The quantities a and b are two nontrivial exponents determined by

$$\lambda = \Gamma^2(1-a)/\Gamma(1-2a) = \Gamma^2(1+b)/\Gamma(1+2b) \ , \quad (0 \le a < \tfrac{1}{2},\ 0 < b \le 1) \ , \tag{4.6}$$

where Γ denotes the Γ function and λ is called the exponent parameter which can be evaluated from the vertices $V^{(i)}$. In the present paper, λ will be considered as a fitting parameter since we do not know the structure of CKN well enough to calculate it from first principles. The scaling frequency ω'_ϵ describes the primary relaxation (α relaxation) in the liquid state, while ω_ϵ describes the secondary relaxation (β relaxation) in both the liquid and glass states. In the simplest MCT model, the F_2 model [1, 2] in which $m_q(t) = V\Phi_q^2(t)$, one finds $\lambda = \frac{1}{2}$, $a = 0.395$, and $b = 1$, and there is consequently no stretching predicted for the α relaxation.

1. First scaling-law regime

In the β-relaxation regime, which exists in the mesoscopic frequency domain between the microscopic frequency Ω and the α-relaxation frequency ω_α, the MCT makes detailed predictions for the scaling law for the density relaxation. Explicitly, the MCT predicts for the dynamical structure factor $S(q,\omega)$ that [3, 33]

$$S(q,\omega)/S_q = (h_q|\epsilon|^{1/2}/\omega_\epsilon)g_\pm(\omega/\omega_\epsilon) \ , \tag{4.7}$$

which is valid for the frequency range $\omega_\alpha \ll \omega \ll \Omega$. In the lowest-order approximation, h_q is a constant which only depends on the wave vector q. The scaling functions $g_\pm$, where $\pm$ refers to $\epsilon > 0$ or $\epsilon < 0$, respectively, depend neither on the separation parameter ϵ nor the wave vector q.

For $(\omega/\omega_\epsilon) \ll 1$ and $(\omega/\omega_\epsilon) \gg 1$, the scaling function $g_\pm$ has the explicit asymptotic forms

$$g_\pm(\omega/\omega_\epsilon) \propto (\omega/\omega_\epsilon)^{-(1-a)} \quad [1 \ll (\omega/\omega_\epsilon) \ll (\Omega/\omega_\epsilon)] \ , \tag{4.8}$$

$$g_+(\omega/\omega_\epsilon) \sim g(0) \quad [0 < (\omega/\omega_\epsilon) \ll 1] , \tag{4.9a}$$

$$g_-(\omega/\omega_\epsilon) \propto (\omega/\omega_\epsilon)^{-(1+b)} \quad [(\omega'_\epsilon/\omega_\epsilon) \ll (\omega/\omega_\epsilon) \ll 1] . \tag{4.9b}$$

Equations (4.8) and (4.9b) indicate the two adjacent power-law regimes in the liquid state, while Eq. (4.8) shows the continuity of the scaled β relaxation in the liquid and glass states. From Eq. (4.7), one obtains the scaling function for the susceptibility [$\chi''(\omega) = \omega S(q,\omega)/S_q$]:

$$\chi''(\omega) = h_q|\epsilon|^{1/2}\hat{\chi}''_\pm(\omega/\omega_\epsilon) . \tag{4.10}$$

Combining Eqs. (4.8), (4.9b), and (4.10) yields a simple interpolation expression for $\chi''(\omega)$ in the region around the minima of the χ'' curves in the liquid state [6],

$$\chi''(\omega) = |\epsilon|^{1/2}[\tilde{A}(\omega/\omega_\epsilon)^a + \tilde{B}(\omega_\epsilon/\omega)^b] \quad (\epsilon < 0) , \tag{4.11}$$

where $\tilde{A}$ and $\tilde{B}$ are constants, independent of the separation parameter and frequency.

The scaling law of Eq. (4.11) implies that the positions of the minima of the $\chi''(\omega)$ curves, $\omega_{\min}$, and the value of χ'' at the minimum, $\chi''_{\min} = \chi''(\omega_{\min})$, are described by the control parameters

$$\chi''_{\min} \propto |\epsilon|^{1/2} , \tag{4.12}$$

$$\omega_{\min} \propto \omega_\epsilon \propto |\epsilon|^{1/2a} . \tag{4.13}$$

Equation (4.11) can be rewritten as

$$\chi''(\omega) = \chi''_{\min}[b(\omega/\omega_{\min})^a + a(\omega_{\min}/\omega)^b]/(a+b) . \tag{4.14}$$

In the ideal glass state below T_c, the explicit form of the susceptibility can be obtained by using Eq. (4.10) with Eqs. (4.8) and (4.9a), which gives

$$\chi''(\omega) = h_q|\epsilon|^{1/2}g(0)(\omega/\omega_\epsilon) \quad [0 < (\omega/\omega_\epsilon) \ll 1] , \tag{4.15}$$

$$\chi''(\omega) = \tilde{B}|\epsilon|^{1/2}(\omega/\omega_\epsilon)^a \quad [1 \ll (\omega/\omega_\epsilon) \ll (\Omega/\omega_\epsilon)] . \tag{4.16}$$

These results indicate that in the ideal glass state the spectral strength of the susceptibility curves scaled in frequency to ω/ω_ϵ is also proportional to $|\epsilon|^{1/2}$, which suggests that $\chi''(\omega_\epsilon)$ should again increase below T_c.

Equations (4.15) and (4.16) imply that there exists a crossover for $\chi''(\omega)$ from linear ω dependence to power-law ω^a dependence. If the crossover point is denoted as ω_e and we designate $\chi''_e = \chi''(\omega_e)$, one can then show from Eqs. (4.15) and (4.16) that

$$\chi''_e \propto |\epsilon|^{1/2} , \tag{4.17}$$

$$\omega_e \propto \omega_\epsilon \propto |\epsilon|^{1/2a} . \tag{4.18}$$

These are the scaling quantities for $T < T_c$.

2. *Second scaling-law regime*

For an ideal kinetic glass transition, ignoring activated hopping processes, α relaxation only exists above T_c. In the α-relaxation region, the scaling is governed by the scaling frequency ω'_ϵ. The scaling law for this region is given by [3]

$$\Phi_q(t) = F_q(t\omega'_\epsilon) , \tag{4.19}$$

where, again, $F_q(t\omega'_\epsilon)$ is a master function which does not depend on the separation parameter ϵ. It has been shown by Götze and Sjögren [8] that the MCT solution of F_q in the α-relaxation regime can be reasonably approximated by the Kohlrausch or stretched-exponential law

$$F_q(t/\tau_\alpha) \propto \exp[-(t/\tau_\alpha)^\beta] . \tag{4.20}$$

From Eq. (4.19), one obtains the scaling function for the susceptibility

$$\chi''(\omega) = \hat{\chi}''(\omega/\omega'_\epsilon) , \tag{4.21}$$

where $\hat{\chi}''(\omega) = \omega\mathrm{Re}\{\mathcal{F}[F_q(t)]\}$ with $\mathcal{F}$ denoting Fourier transformation. From Eqs. (4.20) and (4.21), one can show that the positions of the α-relaxation maxima on the susceptibility curves are controlled by the scaling frequency ω'_ϵ:

$$\omega_{\max} \propto \omega'_\epsilon \propto |\epsilon|^\gamma . \tag{4.22}$$

Equation (4.19) implies one of the most important predictions of the MCT: the stretching of the α relaxation is temperature independent for $T > T_c$. A comprehensive discussion of these and other predictions of the MCT can be found in the review of Götze [3]. Most of the above MCT predictions will be compared with our experimental results in the following sections.

B. Light-scattering mechanism

Until now there has been no well-established theory that could successfully explain the light-scattering mechanism in both liquids and amorphous solids. The *disorder-induced scattering* model for amorphous solids in the formulation of Martin and Brenig [34], though widely cited in the literature, has been found inadequate to explain the low-frequency Raman-scattering results of several amorphous solids [35,36], producing especially serious disagreement for the depolarization ratio. Furthermore, this theory cannot be applied to the liquid state.

In view of the experimentally observed continuous evolution of the low-frequency Raman spectra from a liquid to a glass state, we have recently proposed [35] that the low-frequency light-scattering spectra of liquids and glasses near the glass transition may have a common origin. Specifically, we have suggested that these spectra can be described by the dipole–induced-dipole (DID) interaction-induced scattering theory developed by Stephen [37] for light scattering from liquids. In the DID-only approximation, this theory always leads to a depolarization ratio of $\frac{3}{4}$, which is in good agreement with many of the experimental results on liquids and amorphous solids. (For materials with strong Coulomb

interactions such as the alkali halides, additional interaction terms must be included too, as discussed by Madden [38].)

In Stephen's DID theory, the optical spectrum is given by

$$I(K,\omega) = I_0^{(1)}(\hat{\mathbf{E}}_s \cdot \hat{\mathbf{E}}_0)^2 S(K,\omega) + I^{(2)}(K,\omega) , \tag{4.23}$$

where $\hat{\mathbf{E}}_0$ and $\hat{\mathbf{E}}_s$ are unit vectors of the incident and scattered electric field, K is the magnitude of the scattering wave vector ($\mathbf{K} = \mathbf{k}_0 - \mathbf{k}_s$), and $S(K,\omega)$ is the dynamic structure factor. The first term in Eq. (4.23) is the ordinary first-order scattering equation, which describes Brillouin scattering from the acoustic modes in the low-frequency range. The second term $I^{(2)}(K,\omega)$ is the contribution from second-order scattering, which can be expressed as

$$I^{(2)}(K,\omega) = I_0^{(2)}[1 + \tfrac{1}{3}(\hat{\mathbf{E}}_s \cdot \hat{\mathbf{E}}_0)^2] \times \iint d^3q\, d\omega'\, S(q,\omega')S(|\mathbf{K}-\mathbf{q}|,\omega-\omega') . \tag{4.24}$$

A schematic illustration of this second-order scattering process is shown in Fig. 4(b). In the liquid and glass states, the static structure factor S_q usually shows a sharp peak at $q = q_0$, which corresponds approximately to the average interatomic distance. Therefore it is a reasonable approximation to assume that the integral in Eq. (4.24) is dominated by modes with $q \approx q_0$. Then the second-order scattering contribution can be approximated as

$$I^{(2)}(K,\omega) = BS(q_0,\omega) \otimes S(q_0,\omega) , \tag{4.25}$$

where $\otimes$ denotes convolution over the frequency. It is our interpretation that the experimental depolarized light-scattering spectra shown in Sec. II are due to the second-order scattering described by Eq. (4.25). A similar theoretical result for the light-scattering mechanism was obtained recently from a dielectric model combined with the MCT [39].

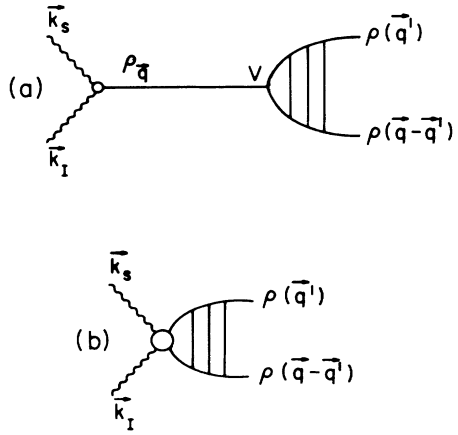

FIG. 4. Schematic illustration of first-order (a) and second-order (b) light-scattering processes. In (b), light scatters directly from two modes with $q \approx q_0$.

To examine the effects of the convolution in Eq. (4.25) and compare with the nonconvoluted $S(q_0,\omega)$, we have performed some numerical analyses by convoluting the numerical $S(q_0,\omega)$ obtained from a MCT calculation with Eq. (4.2) [or equivalently Eq. (4.3)], and also by convoluting the neutron-scattering results of Ref. [11]. A comparison of the curves of the susceptibility $\chi''(\omega) = (\omega/k_BT)S(q_0,\omega)$ and the effective susceptibility $\tilde{\chi}''(\omega) = (\omega/k_BT)S(q_0,\omega) \otimes S(q_0,\omega)$ indicated that the resulting $\chi''(\omega)$ and $\tilde{\chi}''(\omega)$ curves are essentially identical around the minimum region. This result implies that if we treat $\tilde{\chi}''(\omega)$ as if it were $\chi''(\omega)$, ignoring the effects of convolution, the scaling results in the first scaling-law regime (β relaxation) are still valid.

In the second scaling-law regime (α relaxation), the above numerical convolution analyses showed that the α peak on the $\tilde{\chi}''(\omega)$ curve is shifted to a higher frequency but with the same spectral shape as that of the $\chi''(\omega)$ curve. This result can be understood by the following simple interpretation: If we take the approximation of Eq. (4.20), then the convolution effect can be evaluated explicitly by invoking the Faltung theorem:

$$S(q_0,\omega) \otimes S(q_0,\omega) \propto \mathrm{Re}\{\mathcal{F}[\Phi^2(t)]\} \propto \mathrm{Re}(\mathcal{F}\{\exp[-2(t/\tau_\alpha)^\beta]\}) . \tag{4.26}$$

If we define

$$\tau'_\alpha = \tau_\alpha/2^{1/\beta} , \tag{4.27}$$

then

$$S(q_0,\omega) \otimes S(q_0,\omega) \sim \mathrm{Re}(\mathcal{F}\{\exp[-(t/\tau'_\alpha)^\beta]\}) . \tag{4.28}$$

Equation (4.28) indicates that for the α relaxation the convolution just shifts the peak to a higher-frequency position:

$$\omega'_\alpha = 1/\tau'_\alpha = 2^{1/\beta}/\tau_\alpha = 2^{1/\beta}\omega_\alpha . \tag{4.29}$$

If we denote the positions of the α-relaxation maximum on the $\tilde{\chi}''(\omega)$ curve by $\omega'_{\max}$, then according to Eq. (4.29) and the scaling formula Eq. (4.22) we have

$$\omega'_{\max} \propto \omega'_\alpha \propto \omega'_\epsilon \propto |\epsilon|^\gamma . \tag{4.30}$$

Thus, if we treat $\tilde{\chi}''(\omega)$ as $\chi''(\omega)$, the scaling law in the α-relaxation region still applies. Equation (4.29) provides a connection between the light-scattering results and the neutron-scattering (with $q = q_0$) results in the primary relaxation region.

V. DATA ANALYSIS AND DISCUSSION

The experimental results shown in Figs. 1 and 2 exhibit clearly two consecutive relaxation processes at temperatures near and above 100 °C. The crossover frequencies from the low-frequency α relaxation to the mesoscopic frequency β relaxation can be identified as the minima of the $\tilde{\chi}''(\omega)$ susceptibility curves shown in Fig. 2(a). This kind of two-step relaxation process was first ob-

served in dielectric measurements [40–42] and was subsequently found in many other experiments [11, 20–23, 43, 44]. This experimental evidence demonstrates that the two-step relaxation process is a crucial aspect of the dynamics of glass-forming systems. In contrast to other theories of the glass transition, MCT provides a natural explanation for this special character of the structural relaxation process.

A quantitative test of the MCT (for some models) can be carried out by directly comparing the experimental results shown in Figs. 1 and 2 with theoretical spectra (convoluted) obtained numerically by solving Eqs. (4.2) or (4.3) with the MCT kernel of Eq. (4.4). This kind of numerical calculation is currently in progress and will be reported in a future publication. As a more general approach, we have carried out some quantitative tests of the MCT by comparing the scaling-law predictions reviewed in the preceding section with the experimental results in which we treated the $\tilde{\chi}''(\omega)$ results as $\chi''(\omega)$, ignoring the convolution effects so that the MCT predictions can be applied directly, as discussed in the preceding section.

A. The β-relaxation region

1. For $T > T_c$

Since the shape of the susceptibility curves in the β-relaxation region is essentially not affected by the convolution as indicated in the preceding section, the experimental results around the minima of the $\tilde{\chi}''(\omega)$ effective susceptibility curves shown in Fig. 2(a) were analyzed directly using the interpolation function of Eq. (4.14), which, in first approximation, describes the β relaxation for $\epsilon < 0$. In the analysis, $\chi''_{\min}$ and $\omega_{\min}$ were treated as adjustable parameters for each curve. The exponent a was an adjustable parameter for all curves and b was then determined by the constraint of Eq. (4.6). The best fit for all the curves from 110 to 195 °C led to

$$a = 0.273, \quad b = 0.458, \quad \lambda = 0.811 . \tag{5.1}$$

The corresponding $\tilde{\chi}''_{\min}$ and $\omega_{\min}$ values obtained from the best-fit for each temperature are listed in Table I. In Fig. 5, we display the best-fit curves together with the experimental data. The scaling concept is strongly supported by the fact that all the $\tilde{\chi}''(\omega)$ data from different temperatures can be fitted well by a single expression,

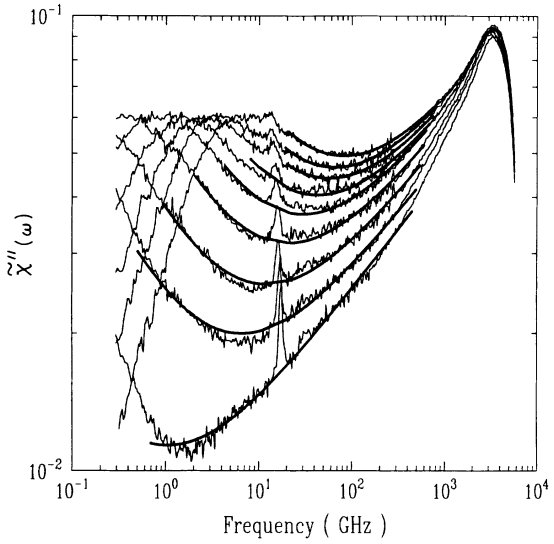

FIG. 5. Best fit of $\tilde{\chi}''(\omega)$ data for $T > T_c$ in the region of the minimum using Eq. (4.14) (thick solid lines) with $\lambda = 0.81$, $a = 0.27$, and $b = 0.46$. The resulting $\tilde{\chi}''_{\min}$ and $\omega_{\min}$ values are listed in Table I. The temperatures are (from top to bottom) 195, 180, 170, 160, 150, 140, 130, 120, and 110 °C.

TABLE I. Scaling quantities for the α and β relaxations obtained from the data analysis (see the text)

$T > T_c$	β relaxation		α relaxation		
T (°C)	$\tilde{\chi}''_{\min}$ (arb. units)	$\omega_{\min}/2\pi$ (GHz)	τ'_α (ns)	$\omega'_{\max}/2\pi$ (GHz)	β
195	0.049	83	0.018	7.1	0.57
180	0.047	67	0.031	4.0	0.58
170	0.044	58	0.043	2.8	0.54
160	0.041	43	0.074	1.6	0.53
150	0.037	30	0.14	0.85	0.53
140	0.032	21	0.35	0.33	0.49
130	0.026	12	1.1	0.12	0.55
120	0.020	6.6	3.1	0.039	0.55
110	0.011	1.1			
$T < T_c$	$\tilde{\chi}''_e$ (arb. units)	$\omega_e/2\pi$ (GHz)			
100	0.0021	0.32			
90	0.0032	2.2			
80	0.0042	7.6			
70	0.0049	17			
60	0.0056	32			
45	0.0062	58			
23	0.0072	100			

Eq. (4.14). This gives the first signature of the scaling property. As a further test, in Fig. 6 we present a rescaled plot of $\tilde{\chi}''(\omega)/\tilde{\chi}''_{\min}$ versus $\omega/\omega_{\min}$. As predicted, all the experimental data around the minima of $\tilde{\chi}''(\omega)$ for different temperatures fall onto a single master curve of the theoretical function of Eq. (4.14) with $\lambda = 0.81$. To demonstrate the sensitivity of the above fitting to the choice of the exponent parameter λ, we have plotted two other theoretical curves for $\lambda = 0.74$ and 0.86 in Fig. 6. The curves of these two λ values are clearly incompatible with the experimental results. Therefore from this fitting we can estimate $\lambda \simeq 0.81 \pm 0.05$.

As a test of consistency, we also tried a fit to the $\tilde{\chi}''(\omega)$ data with both exponents a and b as adjustable parameters. The best fit led to the values $a = 0.269$ and $b = 0.466$, which are essentially the same as those obtained above with the constraints of Eq. (4.6).

For $\epsilon < 0$, the scaling predictions of Eqs. (4.12) and (4.13) imply that

$$(\tilde{\chi}''_{\min})^2 \propto (T - T_c) , \tag{5.2}$$

$$\omega^{2a}_{\min} \propto (T - T_c) . \tag{5.3}$$

A test of these predictions is shown in Figs. 7 and 8 in which we plot $(\tilde{\chi}''_{\min})^2$ and $\omega^{2a}_{\min}$ ($a = 0.273$) versus T (square points in both figures). In both cases the data points indicate excellent linear dependence on T, as predicted. For $(\tilde{\chi}''_{\min})^2$ the best linear fit extrapolates to $T_c = 105\,^\circ$C, while for $\omega^{2a}_{\min}$, $T_c = 98\,^\circ$C; the two values for T_c are in reasonable agreement (ignoring the measurement for $T = 195\,^\circ$C produces T_c values $1\,^\circ$C higher for both cases). These two plots support the scaling-law predictions of the MCT with a statistical significance which is better than that of previous tests for other systems.

As a cross test of the scaling properties, we show in Fig. 9 a double logarithmic plot of $\log_{10}\tilde{\chi}''_{\min}$ versus $\log_{10}\omega_{\min}$ (square points). According to the predictions of Eqs. (5.2) and (5.3), the experimental results should fall on a straight line with a slope of a ($\log_{10}\tilde{\chi}''_{\min} = C_1 + a\log_{10}\omega_{\min}$, where C_1 is a constant). The data points clearly exhibit linear variation and are approximately compatible with the expected slope of

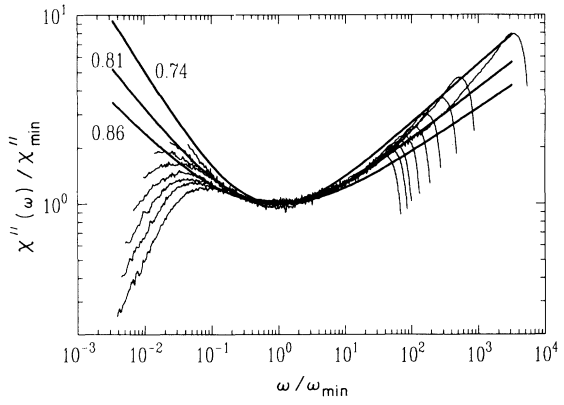

FIG. 6. Rescaled plot of the curves of Fig. 5. The three solid curves are the theoretical results of Eq. (4.14) for (top to bottom) $\lambda = 0.74$, 0.81, and 0.86.

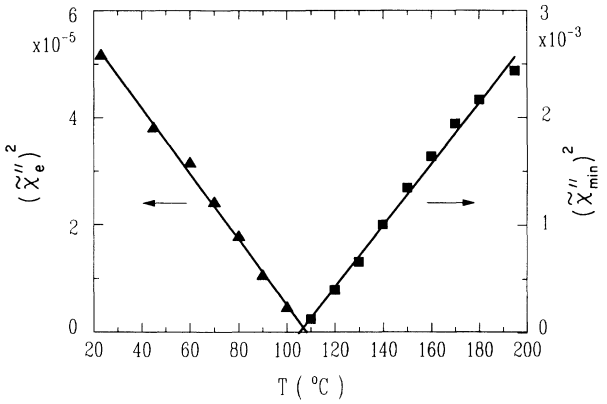

FIG. 7. Temperature dependence of $(\tilde{\chi}''_{\min})^2$ above T_c (square points) and $(\tilde{\chi}''_e)^2$ below T_c (triangular points). The solid lines are linear fits to the data points with $T_c = 105\,^\circ$C for $(\tilde{\chi}''_{\min})^2$ and $T_c = 108\,^\circ$C for $(\tilde{\chi}''_e)^2$.

$a = 0.273$ (dashed line), although there is a discrepancy ($\sim 20\%$) between the best linear-fit slope (0.34) and the expected a value. We notice that this type of discrepancy also exists in other reported experimental studies [21–23].

2. For $T < T_c$

For $\epsilon > 0$, the scaling of the β-relaxation spectra is characterized by the crossover frequency ω_e and the corresponding $\tilde{\chi}''_e$ described in the preceding section. However, from the experimental $\tilde{\chi}''(\omega)$ data shown in Fig. 2(b), the crossover frequencies ω_e for $T < T_c$ do not appear as clearly as the $\omega_{\min}$ appear for $T > T_c$. Furthermore, the MCT in the form discussed in Sec. IV does not correctly describe the α-relaxation dynamics below T_c since activated hopping processes are not included. Therefore it is somewhat more involved to determine the

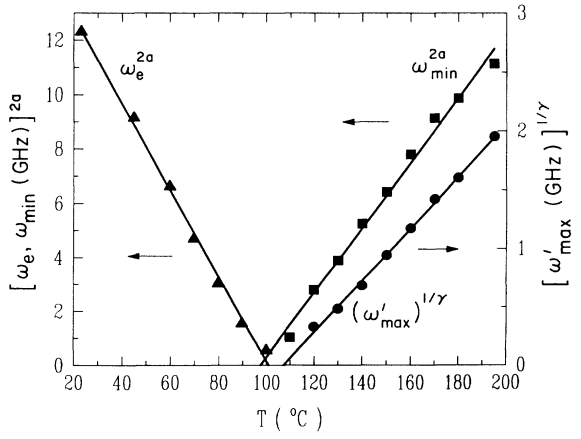

FIG. 8. Temperature dependence of $\omega^{2a}_{\min}$ (squares), ω^{2a}_e (triangles), and $(\omega'_{\max})^{1/\gamma}$ (circles) with $a = 0.273$ and $b = 0.458$. The solid lines are linear fits from which $T_c = 98$, 101, and 107 °C, respectively.

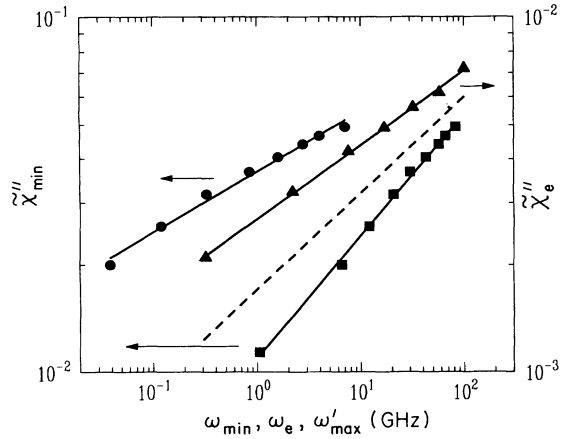

FIG. 9. Double logarithmic plot of $\tilde{\chi}''_{min}$ vs ω_{min} (squares), $\tilde{\chi}''_e$ vs ω_e (triangles), and $\tilde{\chi}''_{min}$ vs ω'_{max} (circles). The solid lines are linear fits with slopes of 0.34 (predicted 0.27), 0.21 (predicted 0.27), and 0.173 (predicted 0.171), respectively. The dotted line with a slope of 0.273 is for comparison.

scaling quantities in this case. As a preliminary attempt, we first rescaled all the $\tilde{\chi}''(\omega)$ curves to fall onto a common master curve. The rescaled curves are shown in Fig. 10. Although this rescaling procedure is less accurate than that for $T > T_c$, the resulting master curve indicates the possibility of describing the β relaxation at different temperatures below T_c by a master function. As demonstrated in the figure, the high-frequency part of the master curve asymptotically joins the power law ω^a with $a = 0.273$ (the solid straight line in Fig. 10). This behavior confirms the continuity of the scaling function for the β relaxation above and below T_c [Eq. (4.8)]. The crossover frequency ω_e and the corresponding susceptibility $\tilde{\chi}''_e$ were then estimated from the rescaling. The values obtained are listed in Table I.

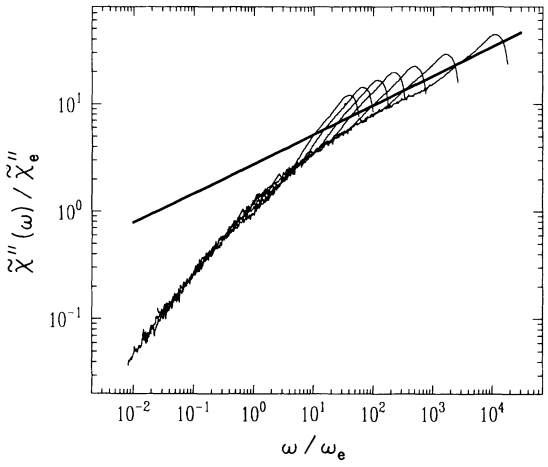

FIG. 10. Rescaled plot of the $\tilde{\chi}''(\omega)$ curves for $T < T_c$ shown in Fig. 2(b). The resulting scale values for $\tilde{\chi}''_e$ and ω_e are listed in Table I. The straight line with a slope of $a = 0.273$ is shown for comparison.

Similar to the $T > T_c$ case, for $T < T_c$ the scales are given by Eqs. (4.17) and (4.18), which can be written as

$$(\tilde{\chi}''_e)^2 \propto (T_c - T) , \tag{5.4}$$

$$\omega_e^{2a} \propto (T_c - T) . \tag{5.5}$$

Tests of these predictions were carried out in the same way as for $T > T_c$. The experimental results for $(\tilde{\chi}''_e)^2$ and ω_e^{2a} ($a = 0.273$) versus T are plotted in Figs. 7 and 8, respectively (triangular points in both figures), together with the high-temperature data. The data again exhibit excellent linear T dependence in both plots. In the first plot, the best linear fit gave $T_c = 108\,^{\circ}\mathrm{C}$ while in the second plot $T_c = 101\,^{\circ}\mathrm{C}$. Both T_c values are in good agreement with the values found from the data above T_c.

It is intriguing to see that the MCT predictions for the temperature dependence of the β-relaxation scaling are well satisfied and the ideal glass transition temperature T_c can be identified from both above and below T_c. These results strongly support the MCT prediction of the existence of a dynamic phase transition at $T_c > T_g$.

A cross test for Eqs. (5.4) and (5.5) is also shown in Fig. 9. The data points of $\log_{10} \tilde{\chi}''_e$ versus $\log_{10} \omega_e$ (triangular points) exhibit linear dependence in agreement with the predicted relation of $\log_{10} \tilde{\chi}''_e = C_2 + a \log_{10} \omega_e$, but again there exists a small deviation ($\sim 20\%$) between the best-fit slope (0.21) and the expected value of $a = 0.273$ (dashed line in Fig. 9). This discrepancy as well as that found for $T > T_c$ may be, in part, a result of ignoring the temperature dependence of the microscopic frequency Ω.

B. The α-relaxation region

Many experimental investigations have shown that the low-frequency α relaxation can be well described by a Kohlrausch law, Eq. (4.20). Theoretical studies also found that the Kohlrausch law is a good approximate solution for the scaling equation in the α-relaxation region.

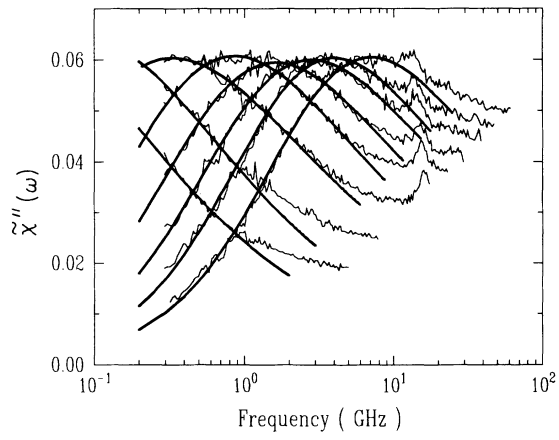

FIG. 11. Best fits of $\tilde{\chi}''(\omega)$ in the α-relaxation region by a Kohlrausch law, Eq. (5.6) (thick solid lines). The resulting τ'_α, ω'_{max}, and β values for each temperature are listed in Table I. The temperatures are (right to left) 195, 180, 170, 160, 150, 140, 130, and 120 °C.

Under the second-order scattering process assumption for the light-scattering mechanism, which leads to the expression of Eq. (4.28), the low-frequency α-relaxation processes shown on the $\tilde{\chi}''(\omega)$ curves [Fig. 2(a)] are described by

$$\tilde{\chi}''(\omega) = (A\omega/k_B T)\mathrm{Re}(\mathcal{F}\{\exp[-(t/\tau'_\alpha)^\beta]\}) , \quad (5.6)$$

where A is a constant.

To obtain the temperature dependence of β and τ'_α, we analyzed the low-frequency data of the $\tilde{\chi}''(\omega)$ curves from 195 to 120 °C by using Eq. (5.6). The best-fitted results (thick solid curves) to the experimental data for each temperature are shown in Fig. 11. In the fitting, A, β, and τ'_α were treated as adjustable parameters for each temperature. The resulting β and τ'_α values are listed in Table I.

From the comparison of the fitted results with the experimental data shown in Fig. 11, one notes the importance of restricting the dynamic range for analyzing the α-relaxation processes so that the influence of the β relaxation can be eliminated.

As emphasized in the Introduction, information on the temperature dependence of the β exponent is a crucial test of the MCT and the percolation theory initially suggested by Campbell [24]. In Fig. 12 we display the temperature dependence of the β values obtained from the above analysis. The results are essentially temperature independent, with $\beta \simeq 0.55$ for $T > T_c$, which provides strong support for the MCT prediction of constant α-relaxation stretching above T_c.

From the above analysis and results, one also finds that in order to obtain reliable information for the low-frequency relaxation processes, observations spanning a wide frequency range and proper handling of the experimental results are extremely important. To demonstrate this point, we show in Fig. 13(a) a conventional analysis for a standard depolarized Brillouin spectrum, which is just a portion of the wide-frequency-range spectrum at 195 °C shown in Fig. 1. The solid curve indicates the best fit to a simple Lorentzian convoluted with the instrumental response function, plus a background. This kind of analysis only involves a small portion of the whole dynamic range and does not distinguish between the two relaxation contributions. Furthermore, the center of the line is blocked by elastic scattering and instrumental resolution. From this conventional analysis, one would be led to the incorrect result of $\beta \simeq 1$.

To illustrate the actual stretching of the α relaxation, in Fig. 13(b) we plot the rescaled results of $\tilde{\chi}''(\omega)/\tilde{\chi}''_{\max}$ versus $\omega/\omega'_{\max}$. Clearly, all the low-frequency experimental data for different temperatures (195–120 °C) fall approximately on a master curve of Eq. (5.6) with $\beta = 0.55$ (solid line). A curve of Eq. (5.6) with $\beta = 1$ is also plotted in the same figure for comparison. Obviously, the simple Debye relaxation implied by $\beta = 1$ is incompatible with the experimental results.

A comparison of the analyses shown in Figs. 13(a) and 13(b) indicates that $\tilde{\chi}''(\omega)$ provides a far more sensitive test for the α-relaxation stretching than the intensity spectra, since the $\tilde{\chi}''(\omega)$ spectra better display the details of the relaxation structure, provided that the frequency window is wide enough to show the whole dynamic process.

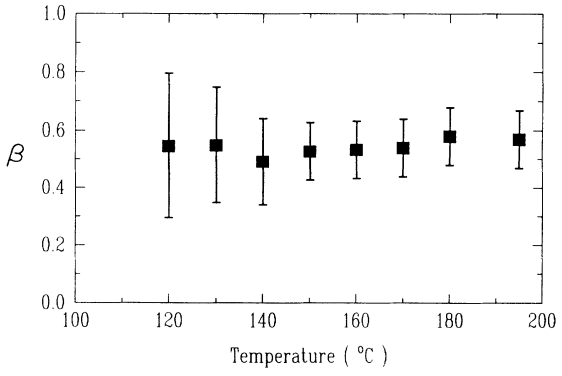

FIG. 12. Temperature dependence of the β values above T_c from the fits shown in Fig. 11.

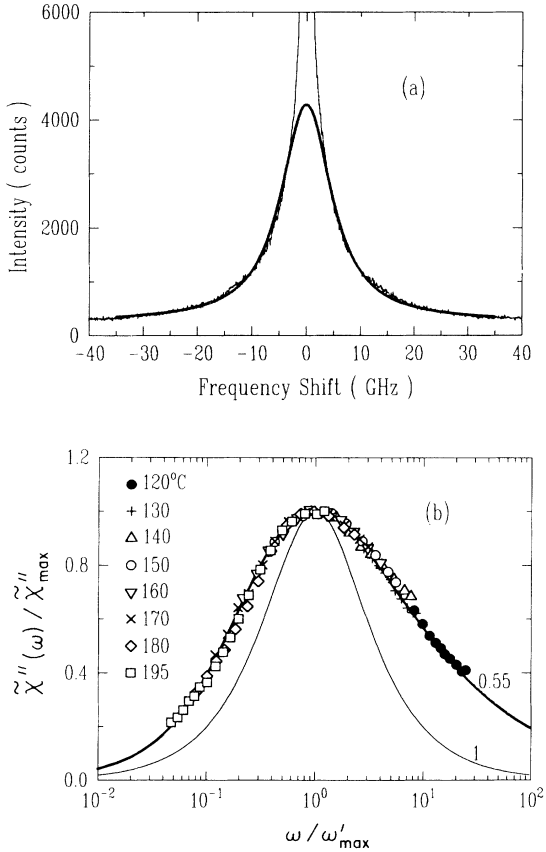

FIG. 13. (a) Depolarized Brillouin spectrum of CKN at 195 °C. The thick solid line is the fit obtained by convoluting the instrumental response with a simple Lorentzian and adding a background. (b) Rescaled plot of $\tilde{\chi}''(\omega)/\tilde{\chi}''_{\max}$ vs $\omega/\omega'_{\max}$ (195–120 °C). The two solid curves are the theoretical results of Eq. (5.6) with $\beta = 0.55$ and 1. Note the obvious disagreement with the Debye $\beta = 1$ prediction of the inner curve.

According to the MCT scaling prediction, the low-frequency α-relaxation scale is given by Eq. (4.30), which can be written as

$$(\omega'_{\max})^{1/\gamma} \propto (T - T_c) . \tag{5.7}$$

A test of this prediction is shown in Fig. 8, in which we plot the data of $(\omega'_{\max})^{1/\gamma}$ versus T (circular points) with $\gamma = 2.92$ [using the values of a and b given in Eq. (5.1)]. It is quite striking to see that the data points again exhibit almost perfect linear temperature dependence with $T_c = 107\,^{\circ}\mathrm{C}$. Again this value is in close agreement with the T_c values found from the analysis of the β relaxation.

A crossover test of the scaling properties for the α and β relaxations can be achieved by plotting $\log_{10}\tilde{\chi}''_{\min}$ versus $\log_{10}\omega'_{\max}$. According to the scaling formulas of Eqs. (4.12) and (4.30), this double logarithmic plot should fall on a straight line with a slope of $1/2\gamma$ ($\log_{10}\tilde{\chi}''_{\min} = C_3 + [ab/(a+b)]\log_{10}\omega'_{\max}$). This prediction is verified by the plot of Fig. 9 (circular points) in which the slope of the straight line fitted to the data points is 0.173, which is essentially equal to the predicted value of $1/2\gamma = 0.171$.

Another crossover test is shown in Fig. 14, in which we plot $\log_{10}\omega_{\min}$ versus $\log_{10}\omega'_{\max}$ (square points). From the predictions of Eqs. (4.30) and (4.13), a linear variation with a slope of $b/(a+b)$ is expected ($\log_{10}\omega_{\min} = C_4 + [b/(a+b)]\log_{10}\omega'_{\max}$), which is approximately correct. A linear fit to the data points gives a slope of 0.49 while the expected value of $b/(a+b) = 0.63$ (dashed line) with a and b is given in Eq. (5.1).

It is particularly interesting to compare the values of τ'_α obtained from this light-scattering study with the τ_α values of the q_0 mode obtained from neutron scattering. In Fig. 15 the upper two full curves indicate the τ_α values obtained from the NSE measurements of Mezei *et al.* [15, 45] (the top one was obtained from our fitting of the extended data of Ref. [45]). The lower two dashed curves are the corresponding results of $\tau_\alpha/2^{1/\beta}$ with $\beta = 0.58$ from Ref. [15]. The circular points are our experimental results for τ'_α from the present light-scattering studies. The τ'_α data points are indeed coincident with the values of $\tau_\alpha/2^{1/\beta}$, as predicted by Eq. (4.27). This result provides additional evidence for the second-order scattering assumption discussed in Sec. IV.

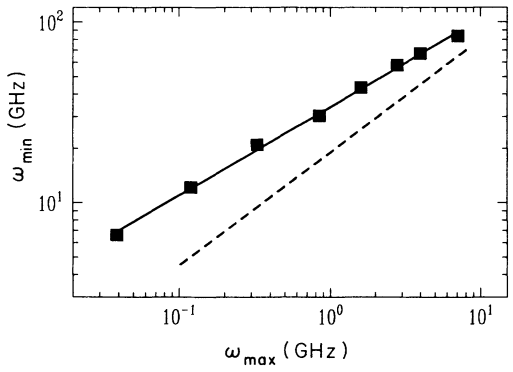

FIG. 14. Double logarithmic plot of $\omega_{\min}$ vs $\omega'_{\max}$. The solid line is a linear fit with a slope of 0.49. The dotted line shows the expected slope of $b/(a+b) = 0.63$ with a and b given by Eq. (5.1).

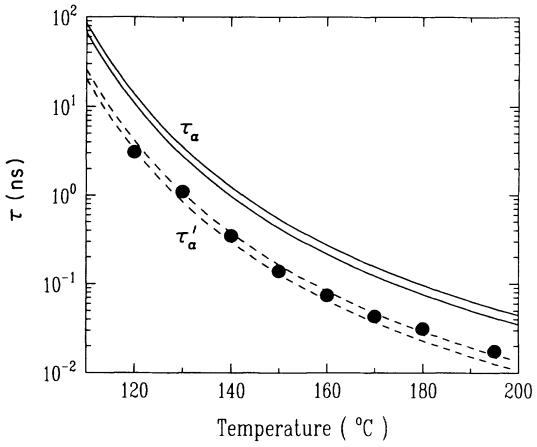

FIG. 15. Comparison of τ'_α with τ_α. The upper two solid curves are τ_α of the q_0 mode found from NSE measurements. The lower two dotted curves are the corresponding values of $\tau_\alpha/2^{1/\beta}$ with $\beta = 0.58$. The circular points are the experimental results for τ'_α from the present light-scattering experiments.

Finally, we plot in Fig. 16 the temperature dependence of the scaling times of the α and β relaxations ($\tau_\beta^- = 1/\omega_{\min}$, $\tau_\beta^+ = 1/\omega_e$). When the temperature approaches T_c from above in the liquid state, the relaxation time τ'_α (circular points) of the α process increases much faster than the scaling time of the β process (τ_β^-) (square points). When the temperature is below T_c, the β-relaxation scale τ_β^+ (triangular points) indicates a rapid slowing down upon heating toward T_c, which is one of the most interesting and counterintuitive predictions of the MCT.

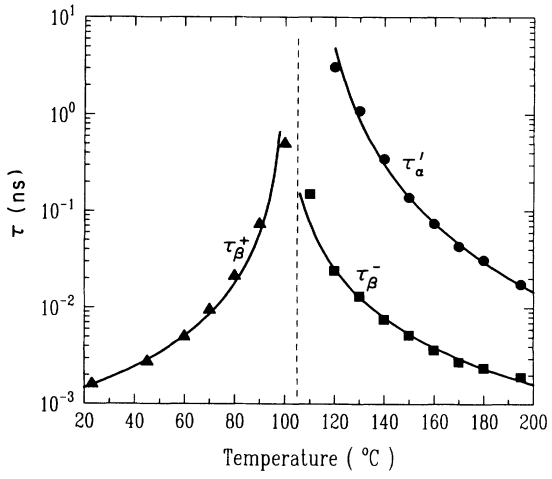

FIG. 16. Temperature dependence of the scaling times of α and β relaxations. $\tau_\beta^- = 1/\omega_{\min}$ (squares); $\tau_\beta^+ = 1/\omega_e$ (triangles); τ'_α (circles).

VI. CONCLUSIONS

Extended light-scattering studies of the glass former CKN have explored the two-step structural relaxation process in the liquid state near T_c. The second-order interaction-induced spectra obtained are similar to the results obtained by neutron-scattering measurements [11].

The α relaxation exhibits rapid slowing down with a temperature-independent stretching parameter $\beta \simeq 0.55$ for $T > 120\,^{\circ}\mathrm{C}$. With increasing temperature, the α relaxation merges with the β relaxation and eventually both relaxations merge with the microscopic excitations. This result supports the MCT prediction for α relaxation above T_c, but it is in contradiction with the percolation theory proposed by Campbell [24, 25], which predicts a continuous increase of β from $\beta = \frac{1}{3}$ at T_g to $\beta = 1$ at high temperatures. (However, β may decrease for temperature below $120\,^{\circ}\mathrm{C}$, the lowest temperature at which it could be determined in our experiments.) We note that the MCT in the form employed here does not include activated hopping processes and therefore makes no predictions about α relaxation below T_c.

The β-relaxation scale was found to exhibit critical slowing down when the temperature approaches T_c from both the liquid and glass states. This phenomenon, which has not been reported previously, to our knowledge, has been observed in the present study and is in agreement with the predictions of the MCT.

Scaling analyses for both the α and β relaxations indicate that the experimental results are generally in good agreement with the scaling-law predictions of the MCT. From these analyses, we obtained a transition temperature of $T_c = 105 \pm 5\,^{\circ}\mathrm{C}$, and an exponent parameter for CKN of $\lambda = 0.81 \pm 0.05$. Our observation that the predictions of the MCT for the β relaxation are fulfilled below T_c as well as above T_c implies that the dynamics of β relaxation are not significantly affected by activated hopping processes.

A comparison of the relaxation time for the α process obtained from this light-scattering study with that obtained from neutron-scattering measurements [15, 45] provided strong evidence for the second-order scattering assumption for the dominant light-scattering mechanism [35].

ACKNOWLEDGMENTS

We thank W. Götze for many helpful suggestions concerning the data analysis and the manuscript, C.A. Angell for several helpful discussions about glasses, and F. Mezei for generously providing unpublished CKN spin-echo data. This research was supported by the National Science Foundation under Grant No. DMR-9014344.

[1] E. Leutheusser, Phys. Rev. A **29**, 2765 (1984).
[2] U. Bengtzelius, W. Götze, and A. Sjölander, J. Phys. C **17**, 5915 (1984).
[3] W. Götze, in *Liquids, Freezing and the Glass Transition*, edited by J.P. Hansen, D. Levesque, and J. Zinn-Justin (North-Holland, Amsterdam, 1991), p. 287.
[4] U. Bengtzelius, Phys. Rev. A **34**, 5059 (1986).
[5] W. Götze, Z. Phys. B **56**, 139 (1984).
[6] W. Götze and L. Sjögren, J. Phys. C **21**, 3407 (1988).
[7] W. Götze and L. Sjögren, Z. Phys. B **65**, 415 (1987).
[8] W. Götze and L. Sjögren, J. Phys. C **20**, 879 (1987).
[9] W. Götze, J. Phys. Condens. Matter **2**, 8485 (1990).
[10] H. De Raedt and W. Götze, J. Phys. C **19**, 2607 (1986).
[11] W. Knaak, F. Mezei, and B. Farago, Europhys. Lett. **7**, 529 (1988).
[12] G.F. Signorini, J.L. Barrat, and M.L. Klein, J. Chem. Phys. **92**, 1294 (1990).
[13] J.L. Barrat, J.N. Roux, and J.P. Hansen, Chem. Phys. **149**, 197 (1990).
[14] J.N. Roux, J.L. Barrat, and J.P. Hansen, J. Phys. Condens. Matter **1**, 7171 (1989).
[15] F. Mezei, W. Knaak, and B. Farago, Phys. Rev. Lett. **58**, 571 (1987).
[16] U. Krieger and J. Bosse, Phys. Rev. Lett. **59**, 1601 (1987).
[17] D. Richter, B. Frick, and B. Farago, Phys. Rev. Lett. **21**, 2465 (1988).
[18] B. Frick, B. Farago, and D. Richter, Phys. Rev. Lett. **64**, 2921 (1990).
[19] W. Petry, E. Bartsch, F. Fujara, M. Kiebel, H. Sillescu, and B. Farago, Z. Phys. B **83**, 175 (1991).
[20] W. Doster, S. Cusack, and W. Petry, Phys. Rev. Lett. **65**, 1080 (1990).
[21] W. Götze and L. Sjögren, J. Non-Cryst. Solids **131–133**, 161 (1991).
[22] L. Sjögren, J. Phys. Condens. Matter **3**, 5023 (1991).
[23] W. Götze and L. Sjögren, Phys. Rev. A **43**, 5442 (1991).
[24] I.A. Campbell, J. Phys. Lett. (Paris) **46**, L1159 (1985).
[25] I.A. Campbell, J.M. Flesselles, R. Jullien, and R. Botet, J. Phys. C **20**, L47 (1987).
[26] I.A. Campbell, J.M. Flesselles, R. Jullien, and R. Botet, Phys. Rev. B **37**, 3825 (1988).
[27] J.M. Flesselles and R. Botet, J. Phys. A **22**, 903 (1989).
[28] C. De Dominicis, H. Orland, and F. Lainée, J. Phys. (Paris) Lett. **46**, L463 (1985).
[29] G. Li, N. Tao, L.V. Hong, H.Z. Cummins, C. Dreyfus, M. Hebbache, R.M. Pick, and J. Vagner, Phys. Rev. B **42**, 4406 (1990).
[30] W.K. Lee, H.Z. Cummins, R.M. Pick, and C. Dreyfus, Phys. Rev. B **37**, 6442 (1988).
[31] C.A. Angell, J. Am. Ceram. Soc. **51**, 125 (1968).
[32] C.A. Angell and D.M. Gruen, J. Phys. Chem. **70**, 1601 (1966).
[33] W. Götze, Z. Phys. B **60**, 195 (1985).
[34] A.J. Martin and W. Brenig, Phys. Status Solidi B **64**, 163 (1974).
[35] N.J. Tao, G. Li, X. Chen, W.M. Du, and H.Z. Cummins, Phys. Rev. A **44**, 6665 (1991).
[36] R.J. Nemanich, Phys. Rev. B **16**, 1655 (1977).
[37] M.J. Stephen, Phys. Rev. **187**, 279 (1969).
[38] P.A. Madden and K. O'Sullivan, J. Phys. Condens. Matter **2**, SA257 (1990).
[39] M. Fuchs and A. Latz, J. Chem. Phys. **95**, 7074 (1991).
[40] G.P. Johari and M. Goldstein, J. Chem. Phys. **55**, 4245 (1971).
[41] G.P. Johari, J. Chem. Phys. **58**, 1766 (1973).

[42] G.P. Johari and M. Goldstein, J. Chem. Phys. **53**, 2372 (1970).
[43] W. Knaak, in *Dynamics of Disordered Materials*, edited by D. Richter *et al.* (Springer-Verlag, Berlin, 1989), p. 64.
[44] N.J. Tao, G. Li, and H.Z. Cummins, Phys. Rev. Lett. **66**, 1334 (1991).
[45] F. Mezei, Non-Cryst. Solids **131**, 317 (1991).